ACOUSTO-OPTIC SCANNING AND REFLECTION SENSING FOR LARGE AREA

OBJECT SEARCH AND RECOVERY

Thesis

Submitted to

The School of Engineering of the

UNIVERSITY OF DAYTON

In Partial Fulfillment of the Requirements for

The Degree of

Master of Science in Electrical Engineering

By

Salaheddeen Giuma Bugoffa

UNIVERSITY OF DAYTON

Dayton, Ohio

August 2016

ACOUSTO -OPTIC SCANNING AND REFLECTION SENSING FOR LARGE AREA

OBJECT SEARCH AND RECOVERY

Name: Bugoffa, Salaheddeen Giuma

APPROVED BY:

____
Monish R. Chatterjee, Ph.D.
Advisory Committee Chairman
Professor
Electrical and Computer Engineering

____
Partha Banerjee, Ph.D.
Committee Member
Professor
Electrical and Computer Engineering

____
Guru Subramanyam, Ph.D.
Committee Member
Department Chair and Professor
Electrical and Computer Engineering

____
Robert J. Wilkens, Ph.D., P.E.
Associate Dean for Research and Innovation
Professor
School of Engineering

____
Eddy M. Rojas, Ph.D., M.A., P.E.
Dean, School of Engineering

ABSTRACT

ACOUSTO-OPTIC SCANNING AND REFLECTION SENSING FOR LARGE AREA OBJECT SEARCH AND RECOVERY

Name: Bugoffa, Salaheddeen Giuma
University of Dayton

Advisor: Dr. Monish R. Chatterjee

Acousto-optic beam steering has been used over the years for a variety of applications [1, 2]. The ability to steer laser beams at high frequencies (tens of MHz to a few GHz) electronically with high angular resolution (given Bragg angles in the mrad range) makes the Bragg cell an ideal device for angular and spatial steering. Lasers are extensively used in many applications such as target detection [3, 4] as well as in ocean depth measurement [5]. In this research, we describe a simple sector-based angular scanning system intended to cover a large surface area in order to identify and spatially locate relatively small objects scattered over the terrain [6]. The scanning system is modeled as a planar surface on the horizontal (XY) plane, with an acousto-optic Bragg cell on board an unmanned aerial vehicle (UAV) operating in the XZ plane. The Bragg cell is excited by a chirped RF signal with frequency ramping from low-to-high or high to-low. As the scanning beam reflects off the horizontal surface, a detector placed on the

UAV picks up the reflected wave (shown to be effective over the scan range), and thereby evaluates the refractive index of the material at the location on the basis of the corresponding Fresnel reflection coefficient [7]. If the surface is, say, primarily sea water, then the detection is considered "negative" unless a material different from sea water is detected. Following each horizontal scan (about 374.15 m) within a sector, the return path is a blank. The Bragg cell, mounted on a stepper motor, is then rotated in the horizontal plane by a small angle, and the second scan run is carried out from the rotated position. Following this process with only L-to-R or R-to-L active scans and interleaving blanks, a "unit" circular sector is scanned with physical dimensions approximately 374.15 m × 300 m. Any "positive" refractive index returned by the sensor is stored in the system in terms of the spatial coordinates of the scanned point. Since the unit sector does not entirely cover a rectangular area or grid, the coverage efficiency can be increased by rotating the Bragg cell from its nominal XZ plane by approximately 90^0 such that it then moves to the YZ plane. Under this configuration, another series of horizontal scans in the XY is carried out, providing additional scanning area that includes portions of the grid previously left out. In reality (as will be discussed) the actual rotation angle is chosen to be 107^0 which allows the scan coverage to be maximal. In this manner, incidentally, some portions of the unit grid may be scanned more than once. This would lead to possible "positive" detection of objects multiple times. The scanning scheme consists of a horizontal row (along Z) reached via multiple grid scans along the Z axis until a chosen scanning distance (about 30 km in this design) is reached, following which the UAV is instructed to reverse direction of flight, and a new row scan is carried out in the reverse direction along an incremental change in Y along the horizontal plane. In this manner, a series of horizontal scans covering an arbitrarily large surface area is carried out (technically over a few hundred square km or the equivalent of a moderate-sized city). The scheme is shown in the numerical simulation to yield coordinate locations of any arbitrary distribution of non-sea-water materials randomly scattered over the scanned surface. This scanning system may be useful in search and rescue applications over large (relatively uniform, homogeneous and planar) surface areas (especially in unreachable terrains directly below the UAV) using the A-O scanning methodology via a Bragg cell mounted on board at an altitude of approximately 8 km.

Dedicated to my parents

ACKNOWLEDGEMENTS

I would like to express my sincere gratitude to my advisor Prof. Monish Chatterjee, who gave me his time and resources in guiding me to complete this research. I greatly appreciate the tremendous support he gave me during the research.

I would also like to express my appreciation to all the faculty members of ECE department from whom I have taken my MSEE course work, which has laid the foundation for my research.

Finally, I would like to thank my Parents, as without their prayers the completion of my graduate studies would have been very difficult.

TABLE OF CONTENTS

LIST OF FIGURES

LIST OF TABLES

CHAPTER 1

BACKGROUND

1.1 Acousto-Optic Diffraction

Acousto-optics (A-O) is basically the interaction between sound and light. A-O diffraction is essentially produced by periodically changing in the refractive index of a homogenous transparent material by propagating an ultrasonic wave through it. The change of refractive index happens because of alternating rarefaction and compression of the material caused by the ultrasonic wave. This change in the refractive index serves as an optical grating moving at the speed of the sound wave in the material which in turn makes the laser beam diffract when it passing through the material [8]. In 1921, Brillouin studied A-O effect and he observed that the diffraction of the light beam occurred when the monochromatic light beam interacted with ultrasonic sound waves [3]. Ten years later, Debye and Sears and Lucas and Biquard experimentally observed the effect of the interaction between sound and light when they used high-frequency sound waves in a liquid to diffract a light beam [9, 10]. They started by normally introducing the monochromatic light beam to a homogeneous, transparent rectangular material [11]. When a high-frequency vibration is applied to the material, it acts as a periodic grating. This high frequency causes variations in the index of refraction. This variation changes sinusoidally through the material with a period of half the acoustic wavelength. The incident light beam is scattered by the variation in the index of refraction, similar to the effect of a grating [12].

The A-O device consists of a piezo-electric transducer that is bonded to the transparent crystal. The generation of an acoustic grating begins with applying an ultrasonic sound wave single into a piezo-electric transducer. The electrical RF source creates a phase grating inside the sound cell. Generally, there are many scattered orders at the A-O output, and the specific type with only two scattered beams (the Bragg regime) is dependent on several parameters including the length of the transducer and the thickness of the crystal. These parameters and others are combined in a figure of merit called the Klein-Cook parameter Q [13]. The value of Q determines diffraction in different A-O regimes, either the Bragg regime operation (which is the one used in this work), or the Raman-Nath regime with multiple diffracted orders. As mentioned, Q should be larger than 8π for Bragg operation [14]. In 1979, Korpel and Poon developed a theory of A-O interaction in which the light and sound waves were represented via plane wave decomposition [15]. This theory leads to the well-known expressions for the diffracted fields in Bragg and Raman-Nath diffraction, and is discussed in detail in Chapter 2.

1.2 A-O Scanning Using Time-Varying RF Frequency

A-O scanning is achieved by moving a laser beam linearly over time across a pre-selected path (say along one axial direction), and then covering incremental distances along the other axis by applying blank return paths) until the surface to be scanned is covered. That is done by diffracting the A-O output laser beam, and then deflecting the beam by using a chirped RF frequency in the acoustic driver. A frequency chirp is a frequency modulated (FM) waveform in which the carrier frequency increases (or decreases) linearly along a ramp. The sound of a siren is a simple example in the audio range. Frequency chirp is widely used in many applications such as radar and sonar systems [16]. The diffracted first-order undergoes a linear deflection due to the chirped RF. The frequency chirp is widely used in A-O scanning for linear laser beam scanning.

1.3 Advantages and Disadvantages of A-O Scanning for Object Location and Recovery.

A-O does not contain any moving parts and therefore it offers high electronically-controlled deflection velocities. This makes the A-O a good choice for a scanning application. A possible disadvantage of the A-O deflector is related to chromatic dispersion. The deflection angle (in this research, a smooth surface is considered which makes the deflection angle equal to the incident angle θ_B) depends on the wave length of the light (λ); hence, the deflector will work fine with monochromatic light. If the laser beam has a broader spectrum (a spread of wavelengths), then different colors will be deflected at different angles (chromatic dispersion) and the deflector may not behave linearly.

1.4 Thesis Organization

This research is organized in five chapters, beginning with a brief background about acoustic-optics (A-O) diffraction, the use of frequency chirp for A-O scanning, and how A-O Bragg conditions and Fresnel coefficients are utilized for search and recovery of dispersed objects. Chapter 2 is an overview of A-O Bragg diffraction and laser scanning, including a discussion of the ideal and non-ideal Bragg cell. Reflections across a 2-D planar surface, evaluations of Fresnel coefficients, and application to a scheme for object research and recovery are explained in Chapter 3. Chapter 4 presents details of the numerical analysis of the scan and recovery schemes and significant results including both types of scanning sectors with precise areas and shapes as well as all sector tracking times, and the total scan time. Also, the minimum and maximum scan angles, the device rotation angles, and the number of sectors needed to cover the desired area are discussed in some detail. The results from the developed MATLAB code to simulate the location and recovery scheme are presented and compare with some real physical values to determine the accuracy of the scan model. Conclusion and possible future work are presented in Chapter 5.

CHAPTER 2

OVERVIEW OF A-O BRAGG DIFFRACTION AND LASER SCANNING

2.1 Introduction

Acousto-optics (A-O) involves the interaction between sound and light used in many applications, including optical phase and frequency modulation, nonlinear feedback and signal processing, and electronic control of the intensity and positioning of a laser beam. When an incident laser beam passes through a Bragg cell it diffracts into many orders. The operation regime is determined based on the magnitude of the dimensionless Klein-Cook parameter Q, as shown in the following formula [17, 18].

$$Q = \frac{4\pi L}{v_s}(f_s \theta_B) = \frac{2\pi L \lambda f_s^{\,2}}{n v_s^{\,2}} \quad , \tag{2.1}$$

where, L is the interaction length, v_s is the sound velocity (typically in range of 2500 to 5000 m/s), f_s is the sound frequency, n is the unmodulated refractive index of the material, ,and θ_B is the so-called Bragg angle. There are two operational regimes of an A-O cell called the Bragg and Raman-Nath regimes. The limits of Raman-Nath and Bragg diffraction have been studied by several authors [19]. In 1996, Chatterjee and Chen showed that for strict Bragg operation Q needs to be greater than 8π [14]. This operation, the so-called Bragg regime of operation, is shown in Fig.2.1. When the light is incident at an angle (θ_B) called the Bragg angle, the incident beam is scattered and generates two orders- the zeroth- and first-orders [20] described in the *upshifted mode* by the following equations,

$$E_0 = E_{inc} \cos\left(\frac{\hat{\alpha}_0 \xi}{2}\right) \quad , \quad \text{and} \tag{2.2}$$

$$E_1 = -j\, E_{inc} \sin\left(\frac{\hat{\alpha}_0 \xi}{2}\right) \quad , \tag{2.3}$$

where $\hat{\alpha}_0$ is the so-called effective phase delay of the light passing through the sound column, and ξ (= z/L with L being the interaction length within the Bragg cell), E_{inc} is the scalar electrical field of the laser beam, E_0, E_1 are the electrical fields of the zeroth- and first-order laser beam respectively.

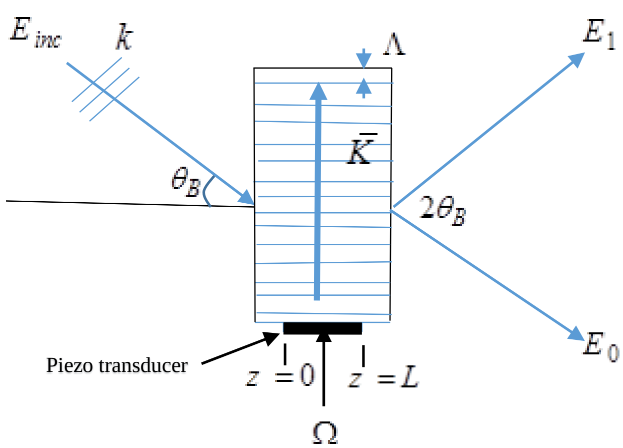

Fig. 2.1 Schematic of input and output laser beams in the Bragg regime.

The diffraction efficiency (η_D) is defined as the ratio of the first-order scattered intensity relative to the incident intensity, and in the perfect Bragg case, is given by:

$$\eta_D = \frac{I_0}{I_{inc}} = \sin^2\left(\frac{\hat{\alpha}_0 \xi}{2}\right) \quad , \tag{2.4}$$

where $\hat{\alpha}_0$ is the so-called effective phase delay of the light passing through the sound column, and ξ (= z/L with L being the interaction length within the Bragg cell) is the normalized distance of propagation with the sound cell as discussed earlier [21, 22]. When Q is much less than 8π (tending towards zero), the system operation is the so-called Raman-Nath regime [23]. The system under this operation generates multiple diffracted orders (……-2 -1 0 1 2 3……) and their amplitudes are given by Bessel functions [24, 25]. The zeroth order follows the direction of the incident light and the diffracted orders are distributed with separation angles of $2\theta_B$ as illustrated in Fig.2.2.

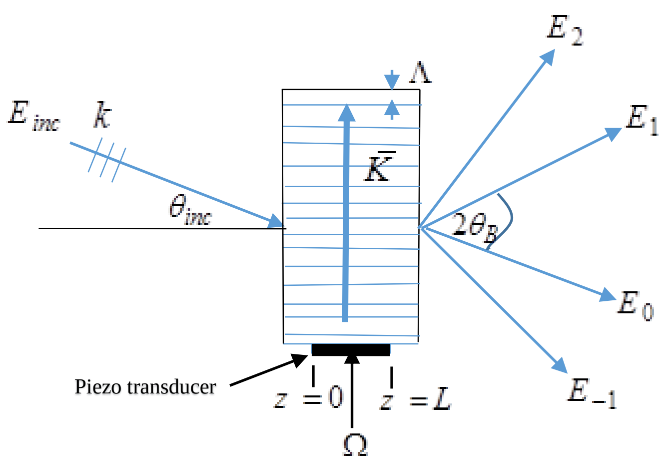

Fig.2.2. Raman-Nath operation regime.

2.2 Bragg Cell Operation and Frequency Chirp Range

A frequency chirp consists of a linear FM wave with the RF frequency varying linearly with time. In this research, the RF frequency (acoustic frequency Ω) is varied between 350 MHz to 1050 MHz, thereby yielding a minimum and maximum Bragg angle. This variation in RF makes the first-order laser beam move from point to point; it starts from the minimum scan angle at 350 MHz and reaches the maximum scan angle at 1050 MHz. The scan, or deflection angle is controlled by the relation

$$\theta_d \equiv \theta_B \approx \frac{\lambda \Omega}{4\pi v_s n} \ ,$$

where, $\Omega/2\pi = f_s$ is the sound frequency in Hz, and v_s is the sound velocity in the Bragg cell. Note that the deflection angle is directly proportional to the sound frequency.

Frequency chirp of linear scan sector takes $1\mu s$ by design to complete, as shown in Fig.2.3 below.

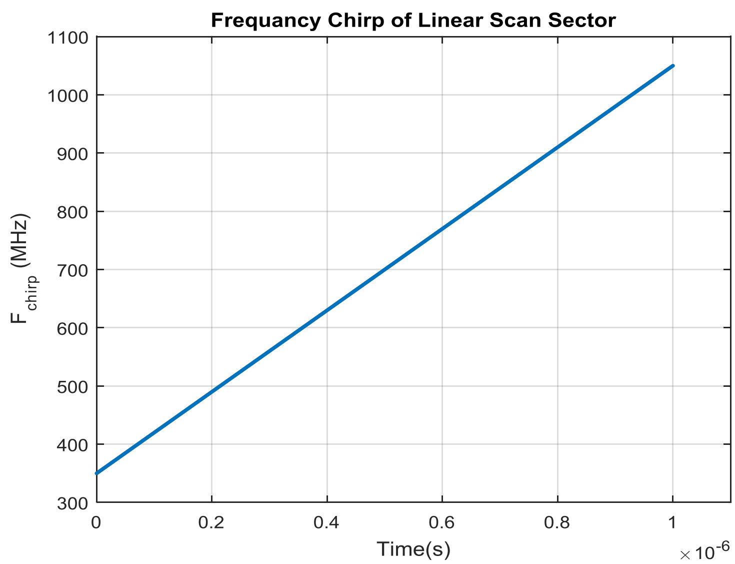

Fig.2.3. Frequency chirp versus time.

This enables the change of the Bragg angle (scan angle) from minimum to maximum to be completed in the same time ($1\mu s$) as shown in Fig.2.4 below. All scan time calculations are shown in detail is in chapter 4.

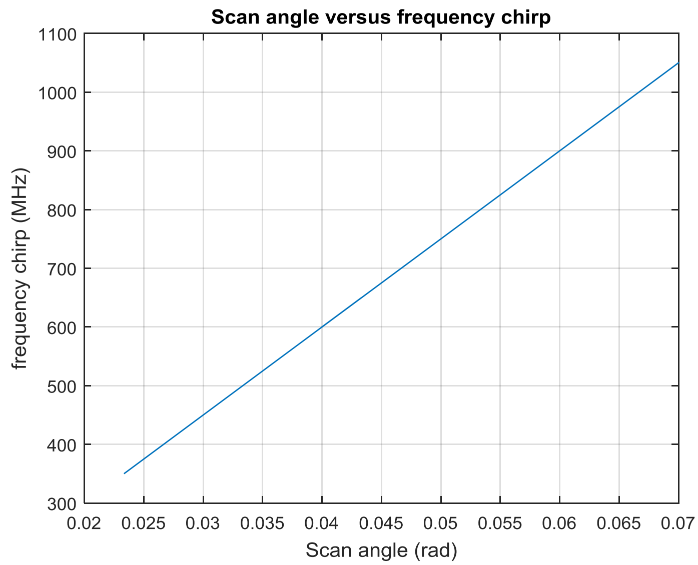

Fig.2.4. Scan angle versus frequency chirp.

When the Bragg cell is excited by a frequency chirp, the first-order beam starts moving linearly with time. Hence, this creates a change in the Bragg angle (i.e., the sweep of E_1) as shown in the Fig.2.5.

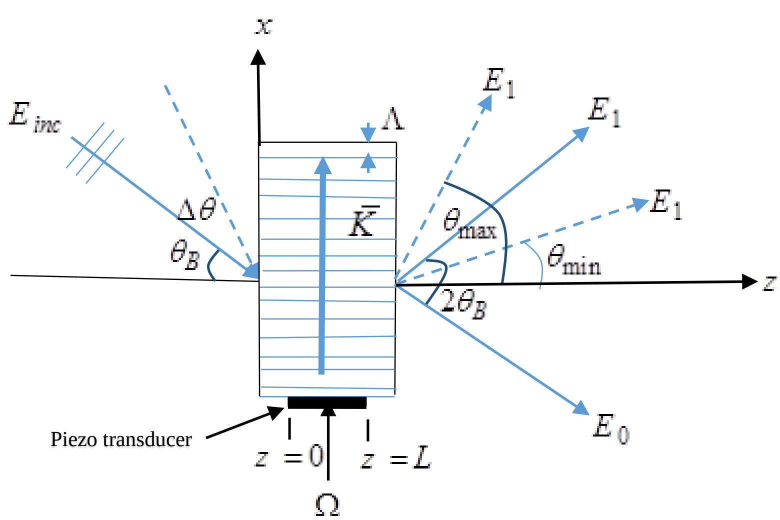

Fig.2.5. Schematic representation of Bragg cell showing input and output deviations.

From Fig.2.5, an A-O Bragg cell with perfect Bragg incidence ($\theta_{inc} = \theta_B$) produces two scattered orders, the zeroth- and first-order (shown by solid lines). Only the first-order diffracted beam is considered, and the incident light is *assumed to be polarized perpendicular* to the plane of incidence. The perpendicular polarization is to ensure there will be no Brewster effect, and therefore will always lead to a reflected wave. It turns out that the effective Bragg angle changes in direct proportion to the RF (sound) frequency ($f_s = \Omega/2\pi$); hence, by changing f_s, the direction of the first-order scattered beam may also be altered. It is this feature that makes it possible to use an acousto-optic modulator as a laser beam deflector and scanner [26]. The change in the value of f_s causes a change in the direction of the scattered light. Ideally, this can happen only on condition that the incident angle is adjusted to the new Bragg angle (otherwise, for a fixed incident angle there is a Bragg mismatch). If the incident angle is fixed, the overall scattering efficiency will decrease. Hence, the operation of an A-O scanner must take the overall loss of efficiency into account if the incident beam is fixed at a specific angle. Moreover, if the Bragg angle changes drastically, the device may no longer operate in the Bragg regime. In this research, the Klein-Cook parameter Q will always be greater than 8π and that guarantees the operation in the Bragg regime. In order to make the condition $Q >> 8\pi$ valid for all RF frequencies, the length of the Bragg cell is chosen to be 5cm. It is clear from eq. (2.1) that Q is proportional to $\Omega\theta_B$, and the values of Q within the chosen Ω-range is found to be:

Table 2.1 Klein-Cook parameter versus RF frequency.

$Q_{\min}$ (350 MHz)	Q_{center} (700 MHz)	$Q_{\max}$ (1050 MHz)
1710	6842	15394

The reason Q increases nonlinearly with Ω (as shown in Fig.2.6 below) is because θ_B is also proportional to Ω, thereby effectively making Q vary as Ω^2. Hence the Qs satisfy the Bragg condition in the entire RF range.

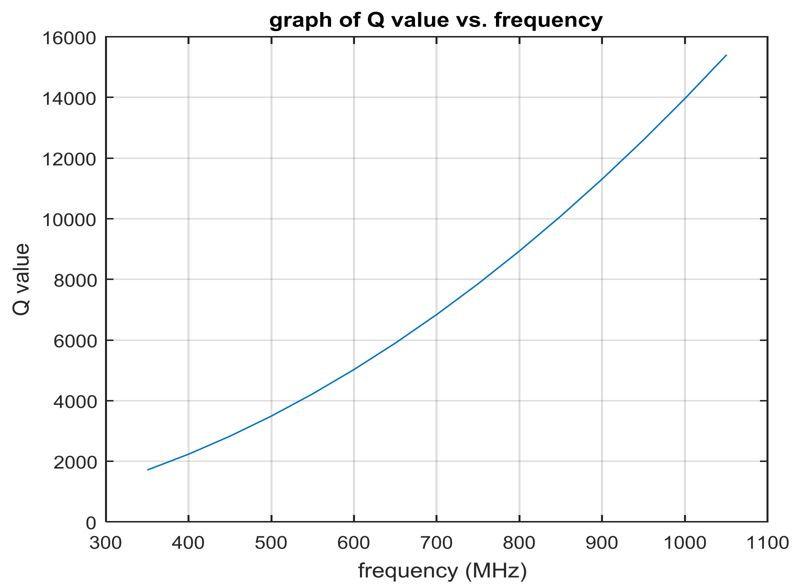

Fig.2.6 Klein-Cook parameter varying nonlinearly with RF frequency.

As seen in Fig.2.6, the Q value increases quadratically with frequency, and is sufficiently high.

CHAPTER 3

REFLECTION ACROSS SURFACES, FRESNEL COEFFICIENTS, AND APPLICATION TO OBJECT SEARCH AND RECOVERY

3.1 Fresnel Coefficients for Perpendicular and Parallel Polarizations

As is known, Fresnel coefficients determine the ratios of the reflected and transmitted electric field amplitudes relative to the incident field amplitude at oblique angles of incidence resolved in terms of perpendicular and parallel polarized components (relative to the plane of incidence, POI) [27]. Consider a linearly polarized plane wave that propagates by angle θ_i relative to the *z*-axis with the wave vector in the XZ plane. The plane of incidence is therefore the XZ plane with the two media (air and seawater, say) separated by the XY plane at $z = 0$. In this research, perpendicular polarization of the electric field is considered for which the reason is discussed further in chapter 4.

A schematic for this arrangement is shown in Fig.3.1.

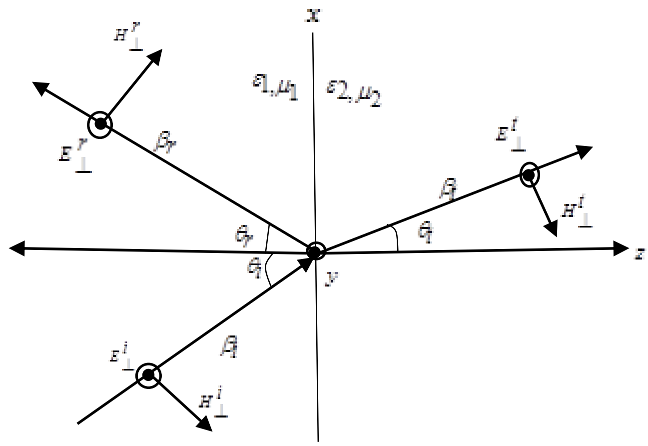

Fig.3.1. Perpendicularly polarized uniform plane wave at an oblique angle at planar interface.

Assuming two dissimilar media, Fresnel reflection and transmission coefficients for the perpendicular polarization are written in the following equations

$$\Gamma_\perp^b = \frac{E_\perp^r}{E_\perp^i} = \frac{\eta_2 \cos\theta_i - \eta_1 \cos\theta_t}{\eta_2 \cos\theta_i + \eta_1 \cos\theta} \quad , \tag{3.1}$$

where, $\Gamma_\perp^b$ is the amplitude reflection coefficient at the boundary; η_1 and η_2 are the wave impedances (= $\sqrt{\frac{\mu_{1,2}}{\varepsilon_{1,2}}}$) in the two media expressible in terms of their permittivities and permeabilities; also, θ_i and θ_t are the angles of incidence and transmission respectively. Hence, $\Gamma_\perp^r = \frac{E_\perp^r}{E_\perp^i} = \frac{\sqrt{\frac{\mu_2}{\varepsilon_2}}\cos\theta_i - \sqrt{\frac{\mu_1}{\varepsilon_1}}\cos\theta_t}{\sqrt{\frac{\mu_2}{\varepsilon_2}}\cos\theta_i + \sqrt{\frac{\mu_1}{\varepsilon_1}}\cos\theta_t}$, and (3.2)

$$T_{\perp}^{b} = \frac{E_{\perp}^{t}}{E_{\perp}^{i}} = \frac{2\eta_2 \cos\theta_i}{\eta_2 \cos\theta_i + \eta_1 \cos\theta_t} = \frac{2\sqrt{\frac{\mu_2}{\varepsilon_2}}\cos\theta_i}{\sqrt{\frac{\mu_2}{\varepsilon_2}}\cos\theta_i + \sqrt{\frac{\mu_1}{\varepsilon_1}}\cos\theta_t} \quad . \tag{3.3}$$

where, $T_{\perp}^{b}$ is the amplitude transmission coefficient. When the light is incident from the rarer to the denser medium $(\varepsilon_2 > \varepsilon_1)$, both reflection and transmission coefficients are always real and for nonmagnetic media the magnitude of the reflection coefficient never vanishes regardless of the $\varepsilon_2 / \varepsilon_1$ ratio or the angle of incidence [27, 28]. When the light propagates from a denser to a rarer medium ($\varepsilon_2 / \varepsilon_1 < 1$) an angle (called the critical angle θ_c) exists as given by eq. (3.4). The value of both the reflection and transmission coefficients become complex when the incident angle exceeds the critical angle (i.e., $\theta_i \geq \theta_c$), and this angle allows total reflection energy at the planer interface.

$$\theta_i \geq \theta_c = \sin^{-1}(\sqrt{\frac{\varepsilon_2}{\varepsilon_1}}), \tag{3.4}$$

On the other hand, when the electric field is parallel to the plane of incidence (POI), then the polarization state is referred to as parallel polarization. In this polarization state, the electric field is parallel to the POI, and the magnetic field is perpendicular to the POI, as shown in Fig.3.2. Note that a smooth interface is assumed in this research.

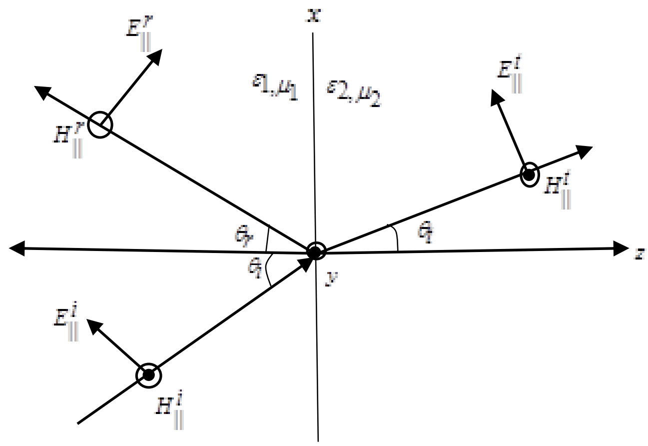

Fig.3.2. Parallel polarized uniform plane wave incident at oblique angle at a planar interface.

The Fresnel amplitude coefficients in this case are given by:

$$\Gamma_{\|}^{b} = \frac{-\eta_1 \cos\theta_i + \eta_2 \cos\theta_t}{\eta_1 \cos\theta_i + \eta_2 \cos\theta_t} = \frac{-\sqrt{\dfrac{\mu_1}{\varepsilon_1}}\cos\theta_i + \sqrt{\dfrac{\mu_2}{\varepsilon_2}}\cos\theta_t}{\sqrt{\dfrac{\mu_1}{\varepsilon_1}}\cos\theta_i + \sqrt{\dfrac{\mu_2}{\varepsilon_2}}\cos\theta_t} \,, \qquad (3.5)$$

$$T_{\|}^{b} = \frac{2\eta_2 \cos\theta_i}{\eta_1 \cos\theta_i + \eta_2 \cos\theta_t} = \frac{2\sqrt{\dfrac{\mu_2}{\varepsilon_2}}\cos\theta_i}{\sqrt{\dfrac{\mu_1}{\varepsilon_1}}\cos\theta_i + \sqrt{\dfrac{\mu_2}{\varepsilon_2}}\cos\theta_t} \,. \qquad (3.6)$$

For this polarization an angle called Brewster angle (θ_{Br}) exists given by eq. (3.7). The reflection coefficient vanishes when the incident angle $\theta_i = \theta_{Br}$. The sign of the reflection coefficient $\Gamma_{\|}^{b}$ varies depending on the relationship between θ_i and θ_{Br} such that when $\theta_i < \theta_{Br}$ the value of $\Gamma_{\|}^{b}$ is negative, and when $\theta_i > \theta_{Br}$ the value of $\Gamma_{\|}^{b}$ is positive; whereas, the value of $T_{\|}^{b}$ is positive for all the values of θ_i .

The Brewster angle is defined as $\theta_i = \theta_{Br} = \sin^{-1}(\sqrt{\frac{\varepsilon_2}{\varepsilon_1 + \varepsilon_2}})$. (3.7)

Note that the above Brewster angle applies strictly for two nonmagnetic media (i.e., $\mu_1 = \mu_2 = \mu_0$).

3.2 Application of Fresnel Reflection Coefficient in Object Search and Recovery.

As mentioned, perpendicular polarization is used for object search and recovery, and the corresponding Fresnel coefficients applied. The laser beam is incident from a UAV at an oblique angle (θ_B) with x-axis in the XZ plane. A schematic view of the scanning system and associated components is shown in Fig.3.3. The scan system model is designed to achieve the main objective which is to detect all materials on the scanned surface (assumed nominally uniform) in the horizontal plane with refractive indices different from the seawater (the search area is assumed to be primarily a large body of water, such as the open sea). Note that this scanning model will generally work only for a uniform background over which arbitrary objects are scattered. The Bragg cell is operated via the use of a chirped RF acoustic source with an initial frequency f_{s1} (here taken as 350 MHz) and a center frequency of 700 MHz; it is ensured that the Bragg cell operates in Bragg or near-Bragg conditions throughout the chirp. The first-order scattered beam will initially hit the surface at an angle of 0.02334 rad; the incident scattered beam will subsequently reach the surface to points along the X-axis (for the first scan line) as the chirp frequency changes. An object may be identified through its refractive index. The surface is considered to be smooth, then the angle of reflection is the same as angle of incidence. All reflected beams (assumed to have Gaussian profiles) will thereafter reach the outer surface of the UAV where a photodetector (PD) will be mounted to intercept the beams. Note that the PD could technically also be mounted inside the UAV- however; this would cause some power loss during propagation through the body of the UAV itself.

In Fig.3.3, z_{i1} and z_{i2} are the scan ranges for the minimum and maximum scan beams relative to the chirp frequencies. Likewise, z_1 and z_2 are the ranges of the reflected beams in the vertical plane corresponding to the minimum and maximum scan locations. Also, $\theta_{\min}$, $\theta_{\max}$ and θ_B are the Bragg angles corresponding to the minimum, maximum and any intermediate chirp frequency. d_s is the linear scan distance that indicate the distance that covered by the laser spot in each linear scan start form minimum scan angle up to reach the maximum scan angle. The reflection laser beams (Gaussian beams) are overlapping in a certain point, and this point which in the high (h) as shown in the figure 3.3 is used to calculate the place of the photodetector as describing in details in chpter.4.

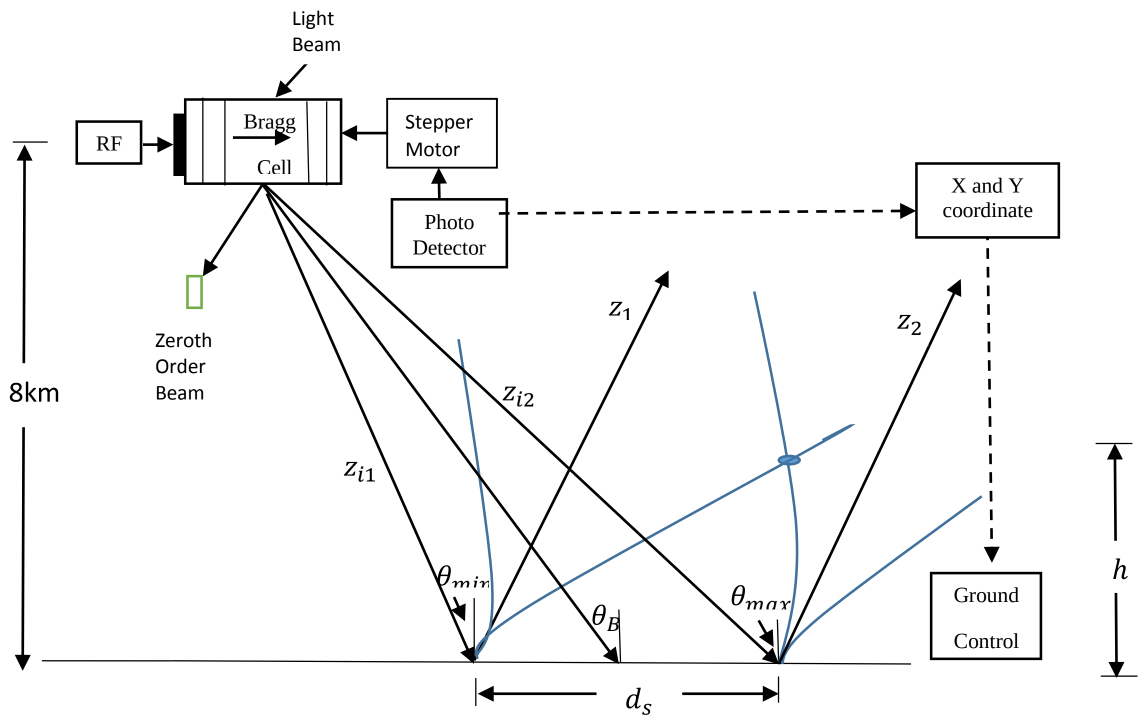

Fig.3.3. Geometrical layout of the scan system model.

CHAPTER 4

NUMERICAL DESIGN OF THE INTEGRATED SCAN, REFLECTION AND DETECTION SCHEME WITH PRIMARY SIMULATION RESULTS

4.1 Physical Considerations for the Scanning System Layout

This chapter includes in-depth numerical analysis that will give a clear picture of the operation of the Bragg cell over the minimum and maximum Bragg angles as well as the scan distance. Assumptions for and some limitations of the scan logarithm are stated, and the optimal placement of the photodetector above the ground plane in order to intercept the reflected wave in the entire scan range is determined from the physics and geometry of the system. A sector-based angular scanning system intended to identify and spatially locate relatively small objects scattered over a large terrain is the main purpose of the research. The system is modeled as a planar surface on the horizontal (XY) plane, with an acousto-optic Bragg cell on board an UAV operating in the XZ plane. The Bragg cell is excited by a chirped RF signal with a designed frequency ramp. As the scanning beam reflects off the horizontal surface, a detector placed strategically at a suitable altitude (in the analysis shown to be on board the UAV itself) picks up the reflected wave and thereafter evaluates the refractive index of the material at the location using the Fresnel reflection coefficient. For large area coverage, the UAV makes alternate 180-degree turns at the end of each row-scan, thereby after several row scans a net surface area is covered in the XY plane.

4.2. Schematic Scanning Configuration

The scan system is modeled to cover an area of 30 km by 30 km, the dimensions of a mid-size city. Two sectors are created to cover a maximal amount of the area within a unit cell. The unit cell is created by changing the sound frequancy which is concedre in the current application, the RF frequency (Ω) is varied between 350 MHZ to 1050 MHZ with center frequency of 700MHz, thereby yielding a minimum and maximum Bragg angle.

$$\theta_B = \frac{\lambda\Omega}{4\pi v_s n} \ ,$$

where the sound velocity v_s is assumed to be 3 km/s and $n = 1.5$,

$$\theta_{\min} = \frac{\lambda\Omega_{\min}}{4\pi v_s n} = 0.02334 \text{ rad}, \quad \theta_0 = \frac{\lambda\Omega_0}{4\pi v_s n} = 0.0467 \text{ rad, and } \theta_{\max} = \frac{\lambda\Omega_{\max}}{4\pi v_s n} = 0.07 \text{ rad.}$$

The laser beam waist radius at the Bragg cell output (w_0) is calculated based on a 1m beam spot size on the ground from an altitude of 8km using:

$$z = z_0\sqrt{(\frac{w}{w_0})^2 - 1}\,,$$

where, where z is the propagation distance from the output plane of the Bragg cell. Also,

$$z^2 = z_0^2(\frac{w^2 - w_0^2}{w_0^2})\text{, so that}$$

$$z^2 w_0^2 + z_0^2 w_0^2 = z_0^2 w^2\text{, and}$$

$$w_0^2 = \frac{z_0^2 w^2}{(z^2 + z_0^2)} \quad . \tag{4.1}$$

In addition, $w_0 = \sqrt{\frac{z_0\lambda}{\pi}}$, where λ is the optical wavelength, with depth of focus

$$z_0 = \frac{w_0^2 \pi}{\lambda} \quad . \tag{4.2}$$

By solving eqs. (4.1) & (4.2) for z_0 & w_0 , we get $w_0 = 0.0015m$ & $z_0 = 12.1423m$.

The minimum and maximum Bragg angles directly translate in the scanning system to the minimum and maximum scan angles of incidence on the surface to be scanned. These angles represent the limits of the scanning beam over a spatial distance (d_s) in the horizontal (XY) plane as depicted in Fig.4.1.

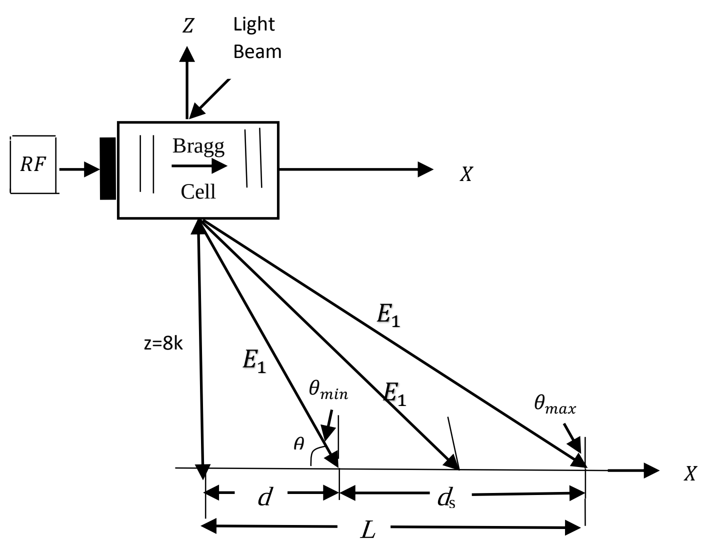

Fig.4.1. Bragg cell layout and relative orientation of first-order Bragg diffraction with minimum and maximum incident angles and scanning distance.

In the above scheme,

$\theta_{\min} = 1.3373^o$ & $\theta_{\max} = 4.0107^o$

$\theta = 180 - (90 + \theta_{\min}) = 89.66^o$

$d = z * \tan\theta_{\min} = 186.75m$

$L = z * \tan\theta_{\max} = 560.9m$

$d_s = L - d = 374.15m$

The first sector is a *horizontal* sector as shown in Fig.4.2. The sector is created by executing linear scans per line of about 374.15 m, and generating additional scan lines by rotating the Bragg cell, mounted on a stepper motor, in the XZ plane. As the figure shows, such a forward scan leaves a sizable part of the unit cell outside the sector. Following coverage of the first sector, the Bragg cell is rotated by 107^0 and the second sector is scanned, thereby reducing the unscanned area within the unit cell. The spot size of the laser beam on the scanned surface is designed to be 1 m, and moves horizontally by 0.5 m steps. In this manner, the unit cell coverage is about 374.15 m × 300 m. Since some of the scanned areas within the two sectors actually overlap, this implies that some of the scanned "objects" may actually be scanned more than once. The scanned area coverage using two sectors approaches close to 100%.

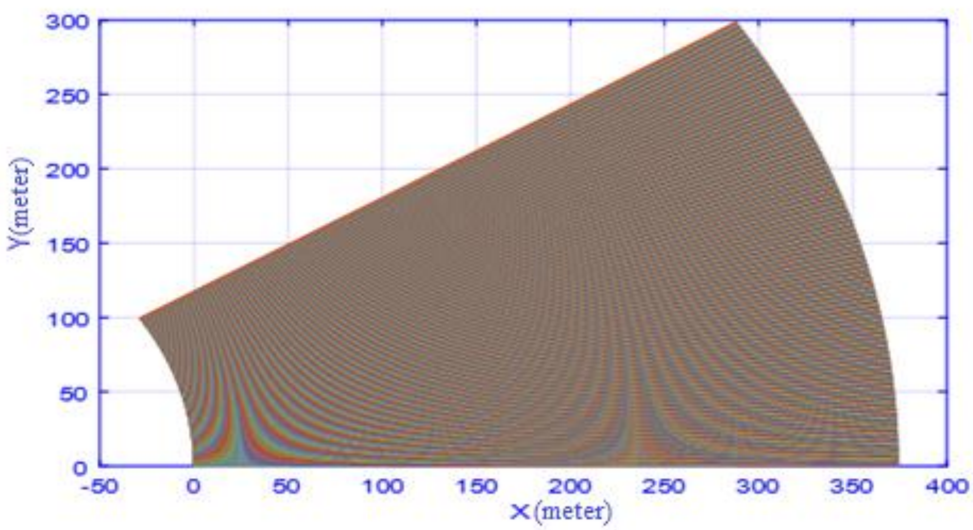

Fig.4.2. Horizontal sector scan layout in unit cell.

In Fig.4.2, the sector shown is created in the XY plan by moving the laser spot from the first point (0, 0) by a distance of 0.5 m until the last point at (374.15, 0) is reached, successively changing the incident angle. The return path is a blank; the scan system including the Bragg cell and the laser source mounted on a stepper motor is rotated by a small angle counter clockwise while the RF source is reset to 350 MHz. This process is then continued until the horizontal sector is completed. The uncovered area from the horizontal sector is then covered by a vertical sector created by rotatting the scan system by 107^0 degree counter clockwise. In each return the scan system will rotate a by very small angle clockwise within this time (blank time) as shown; the vertical sector is shown in Fig.4.3.

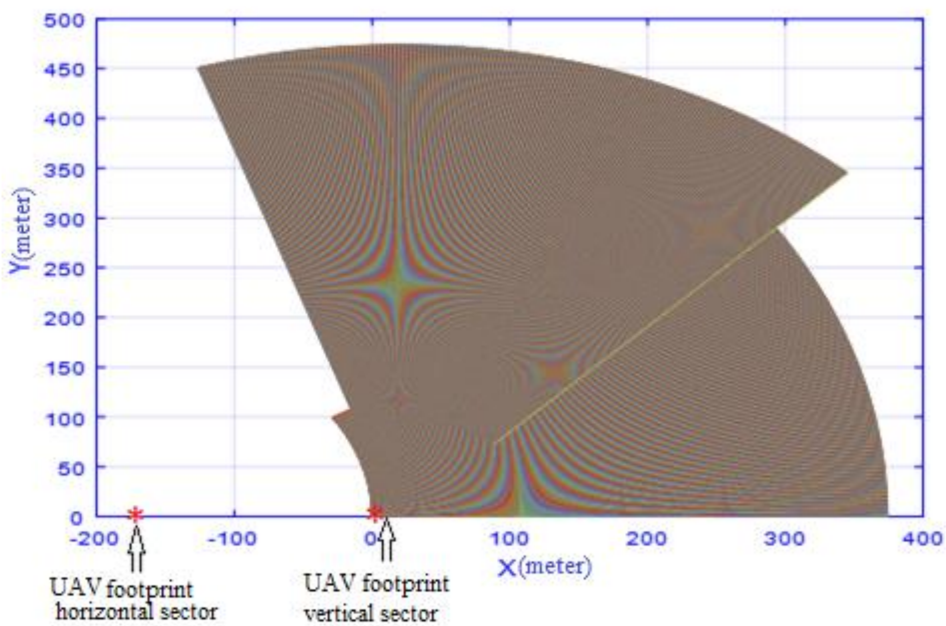

Fig.4.3. Vertical and horizontal sector layout in unit cell.

As can be seen in Fig.4.3, there is overlapping area between the two sectors. Any object located within the overlapping area will be therefore detected twice and ground control (to which the UAV will transmit sensor coordinates) will receive the coordinates for the detected object twice. The UAV is placed at a height of 8 km above the horizontal plane, and begins the scan process at a location 186.75m behind the "zero" of the scanned unit cell. This distance arises from the minimum incident angle (0.02334 rad). The scanning system requires several time conditions to be properly met in order to execute the object detection goals set up for this work. Details of all the critical times are discussed further in this chapter.

4.3. Optimizing Photodetector Location

After careful analysis, the optimal placement of the photodetector is determined to be on the UAV itself. This determination was made using the following set of equations used to calculate the approximate intersection point between the reflected Gaussian-profile beams from the minimum and maximum angular positions.

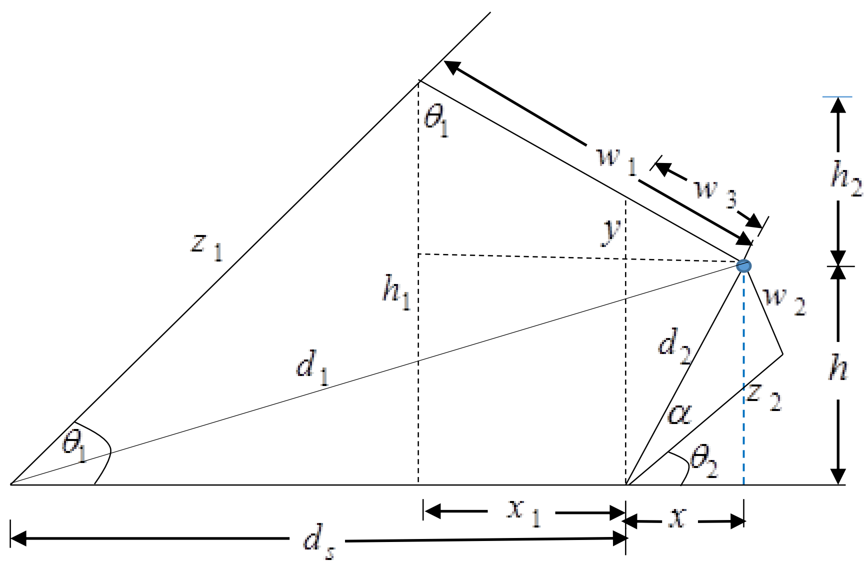

Fig.4.4. Geometric illustration of the intersection point at height *h* above the horizontal plane.

In Fig.4.4, z_1 and z_2 represent the physical propagation distance of the reflected Gaussian beams from the minimum and maximum incidence points; w_1 and w_2 are the corresponding beam spot sizes corresponding to the point of intersection of the two Gaussian beams (the right edge of beam 1 and the left edge of beam 2), here linearly connected by d_1 and d_2, as shown. The angles θ_1 and θ_2 are complementary to the minimum and maximum angels of incidence. α represents the divergence angle of the Gaussian beam. *h* is the vertical height where the two beams intersect, and would represent the minimum altitude where the photodetector would have to be placed in order to intercept the reflected beams across the scan area. From the figure, we find

$$d_2^2 = (w_2^2) + (z_2^2) \quad , \tag{4.3a}$$

$$h_1 = z_1 \sin\theta_1 \;\&\; h_1 = h + h_2 \ , \tag{4.3b}$$

$$h = d_2 \sin(\theta_2 + \alpha) \ \text{, and}$$

(4.3c)

$$\tan\alpha = \frac{w_2}{z_2} \quad . \quad \text{Note that} \tag{4.3d}$$

$\theta_1 = 90 - \theta_{\min,} \theta_2 = 90 - \theta_{\max}$ and $\alpha =$ divergence angle of the laser beam. Also,

$$h_2 = w_1 \cos\theta_1 \quad , \tag{4.3e}$$

$$w_1^2 = w_0^2 (1 + \frac{\tilde{z}_1^2}{z_0^2}) \quad \text{, and} \tag{4.3f}$$

$$w_2^2 = w_0^2 (1 + \frac{\tilde{z}_2^2}{z_0^2}) \, . \tag{4.3g}$$

From Fig.3.3,

$$\tilde{z}_1 = (z_1 + z_{i1}) \,\&\, \tilde{z}_2 = (z_2 + z_{i2}) \ ,$$

$$\frac{x}{x + x_1} = \frac{w_3}{w_1} \ ,$$

$$x^2 = d_2^2 - h^2 \ ,$$

$$x_1 = d_s - z_1 \cos\theta_1 \ ,$$

$$\frac{\sqrt{d_2^2 - h^2}}{\sqrt{d_2^2 - h^2} + d_s - z_1 \cos\theta_1} = \frac{w_3}{w_1} \ ,$$

$$w_3 = \frac{x}{\sin\theta_1} \Rightarrow \frac{\sqrt{d_2^2 - h^2}}{\sqrt{d_2^2 - h^2} + d_s - z_1 \cos\theta_1} = \frac{x}{w_1 \sin\theta_1} \ , \text{ and}$$

$$\sqrt{d_2^2 - h^2} + d_s - z_1 \cos\theta_1 = w_1 \sin\theta_1 \ .$$

Since, $\sqrt{d_2^2 - h^2} = w_0$ and $d_s >> w_0$ we obtain

$$d_s = w_1 \sin\theta_1 + z_1 \cos\theta_1 \ , \tag{4.3h}$$

$$d_2 = \sqrt{(w_2^2 + (z_2^2))} \Rightarrow d_2 = \sqrt{w_0^2 [1 + \frac{z_2^2}{z_0^2} + \frac{z_2^2}{w_0^2}]} \ , \tag{4.3i}$$

$z_0 >> w_0$, and

$$d_2 = \sqrt{w_0^2 + z_2^2} \ . \tag{4.3j}$$

From the above set of equations, we finally obtain:

$$w_0 = 0.0015m \;\&\; \theta_2 = 1.5683 rad$$

The value of h is found to be $h = 1.5mm$. This negligibly small number implies that *any* detector placed above the horizontal plane should be able to intercept the reflected beams across the entire scanning area. Therefore, placing the photodetector on board the UAV should yield acceptable results.

4.4. Photodetector Sensitivity Considerations

The photodetector must be designed so that it is sensitive enough to capture the incident light even after it has undergone loss of power due to (i) the Bragg cell efficiency, and (ii) the power reflection coefficient from the reflection on the ground across the scanning distance. Accordingly, we begin by considering the Bragg cell scattering efficiency under non-ideal conditions due to deviations from the actual Bragg angle when the RF frequency changes and the incident light beam is fixed at the Bragg angle for the center RF frequency (700 MHz). The first-order efficiency is given by [29]

$$\eta_D = \frac{(\frac{\hat{\alpha}_0}{2})^2}{(\frac{\delta Q}{4})^2 + (\frac{\alpha_0}{2})^2} \times \sin^2(\sqrt{(\frac{\delta Q}{4})^2 + (\frac{\alpha_0}{2})^2}), \text{ where} \tag{4.4a}$$

η diffraction efficiency,

$\delta\theta_B$ deviation of the incident light from the Bragg angle,

$\hat{\alpha}_0$ peak phase delay, and

Q Klein-Cook parameter.

Based on the parameters chosen, the Bragg angle deviation is found to be,

$\delta = \frac{\Delta\Omega_s}{\Omega_{sc}} = \frac{\Delta f_s}{f_{sc}}$, where Δf_s is the frequency deviation and f_{sc} is the sound frequency at the center of the chirp. Note that the above implies that δ varies over the range ± 0.5. The peak phase delay is chosen to be $\hat{\alpha}_0 = 51\pi$ (which usually implies a strong level of acoustic power); the efficiency is found as listed in Table.4.1. Specifically, the δQ term in the sinc^2-type efficiency defined in eq.(4.4a) takes the frequency dependence:

$$\delta Q = \left(\frac{f_s - f_{sc}}{f_{sc}}\right)\left(\frac{2\pi L\lambda}{n{v_s}^2}\right){f_s}^2, \tag{4.4b}$$

Table.4.1 Diffraction efficiency varying with frequency.

$\eta_{D(\min)}\big\|_{350MHz}$	$\eta_{D(center)}\big\|_{700MHz}$	$\eta_{D(\max)}\big\|_{1050MHz}$
8.9138%	100%	0.0016%

Clearly, the diffraction efficiency is highly sensitive to frequency. The diffraction efficiency is found to be maximum at center frequency (700 MHz) corresponding to perfect Bragg incidence ($\theta_{inc} = \theta_B$).

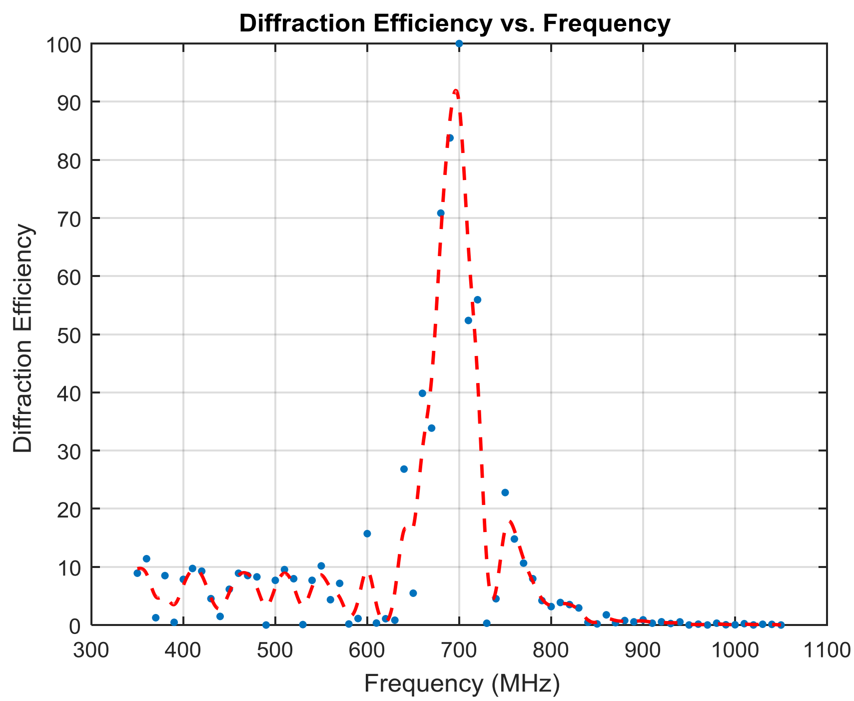

Fig.4.5 Diffraction efficiency varying with sound frequency.

The choice of $\hat{\alpha}_0$ above needs some further explanation. We note from eq. (4.4a) that since Q for this problem is fairly high, the efficiency of the Bragg cell would be very low unless one chooses to operate the cell at sufficiently high $\hat{\alpha}_0$. We note also that the chosen $\hat{\alpha}_0$ has to be an odd multiple of π, such that even under zero deviation, we obtain the maximum value of the sine term in eq. (4.4a). Technically, one could pick an arbitrarily large (odd) value of $\hat{\alpha}_0$; however, we note that $\hat{\alpha}_0$ depends directly on the applied RF or acoustic power from the sound cell driver. Hence, there is a physical limit to the value of $\hat{\alpha}_0$ that is permissible under the RF power limitations of the source. We note that even with this choice of $\hat{\alpha}_0$, the efficiencies achieved are still rather low (from about 2% to about 20%). From this perspective, it appears that the value 51π may place the required source power in the permissible range. Next, we note that under reflection from a planar surface with perpendicularly polarized light (whose rationale explain below), the power reflection coefficient is given by

$$\frac{s^{ref}{}_{avg}}{s^{i}{}_{avg}} = \left|\Gamma_{\perp}\right|^{2} \quad , \tag{4.4c}$$

where, $s^{ref}{}_{avg}$, $s^{i}{}_{avg}$ are reflected and transmitted power densities, and $\Gamma_{\perp}$ is the Fresnel amplitude reflection coefficient for perpendicular polarization.

Note that the Fresnel amplitude reflection coefficient for perpendicular polarization is given by:

$$\Gamma_{\perp} = \frac{\eta_2 \cos\theta_i - \eta_1 \cos\theta_t}{\eta_2 \cos\theta_i + \eta_1 \cos\theta_t} \quad , \tag{4.4d}$$

where η_1 and η_2 are the wave impedances ($= \sqrt{\frac{\mu_{1,2}}{\varepsilon_{1,2}}}$) in the two media, expressible in terms of their permittivities and permeabilities; also, θ_i and θ_t are the angles of incidence and transmission respectively. For *nonmagnetic* (μ_r = 1) media, the above equations reduce to:

$$\Gamma_{\perp} = \frac{n_1 \cos\theta_i - n_2 \cos\theta_t}{n_1 \cos\theta_i + n_2 \cos\theta_t} \quad , \tag{4.4e}$$

where, n_1 and n_2 are the (phase) refractive indices of the two media. Also, $\Gamma_{\perp}$ is calculated by invoking Snell's law generalized as follows:

$$\beta_1 \sin\theta_i = \beta_2 \sin\theta_t \quad , \tag{4.4g}$$

where, β_1 and β_2 are the unbounded wavenumbers $(= \omega\sqrt{\mu_{1,2}\,\varepsilon_{1,2}})$ in the two media where ω is the radian optical frequency.

The reason for choosing perpendicularly polarized light for the scanning problem is to avoid any possible Brewster condition during the reflection from the scanned surface, since the detection of the reflecting material is based on measuring the reflected light.

With the above two conditions, one obtains the power incident at the photodetector as:

$P_D = P_{inc}\ p$, where p is a figure of merit.

Based on the above, with an incident laser power at the input of the Bragg cell being, say, 25 mW, the resulting reflected power reaching the photodetector may be readily calculated. This number, of course, will change due to the change of the RF frequency, and also the incident angle at the interface which is the same as the corresponding Bragg angle of operation. This in turn changes the Fresnel power coefficient. We note at this stage that the reflected power in this problem varies nonlinearly with the product $\eta_D\,|\Gamma_\perp|^2$. Table 4.2 shows in detail the Bragg angles, Fresnel coefficients, diffraction efficiencies, the figure of merit *p*, and the photodetector power for four different materials plastic, copper, aluminum, and glass as an example. Similar tables are needed in order to establish the range of possible photodetector power levels across a range of chosen nonmagnetic materials.

Table 4.2. Reflected power from air- plastic interface incident at the photodetector.

$\Omega(MHz)$	$\theta_B = \theta_i$	$\eta_D\,\%$	$\Gamma_\perp$	$p = \eta_D \lvert\Gamma_\perp\rvert^2$	$p_D\,(\mu w)$
350	0.0233	8.9138	-0.1969	0.003455	86.3884
400	0.0267	7.8545	-0.1969	0.003455	76.1393
450	0.0300	6.1539	-0.1969	0.002386	59.6694
500	0.0333	7.6849	-0.1970	0.002981	74.5350
550	0.0367	10.1700	-0.1970	0.003946	98.6689
600	0.0400	15.7159	-0.1970	0.006101	152.5270
650	0.0433	5.4750	-0.1971	0.002126	53.1566
700	0.0467	100.0000	-0.1971	0.038851	971.2820
750	0.0500	22.7839	-0.1971	0.008855	221.3913
800	0.0533	3.1709	-0.1972	0.001233	30.8258
850	0.0567	0.1915	-0.1972	0.000074	1.8624
900	0.0600	0.8881	-0.1973	0.000345	8.6429
950	0.0633	0.0086	-0.1973	0.000003	0.0834
1000	0.0667	0.0433	-0.1974	0.000016	0.4220
1050	0.0700	0.0016	-0.1975	0.0000006	0.0155

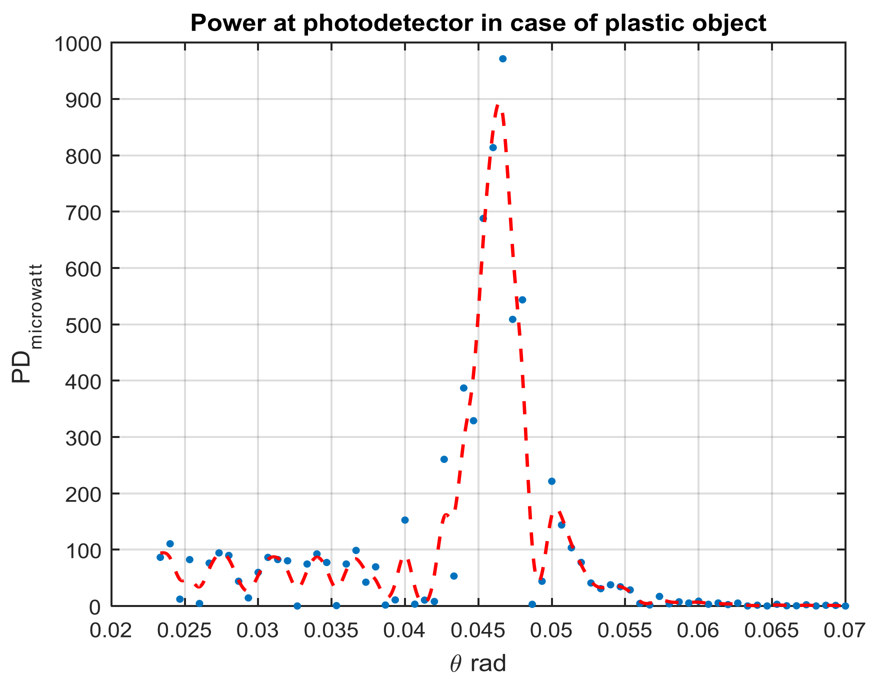

Fig.4.6. Power at the photodetector versus the scan angle for the case of plastic.

The same calculation is carried out for the power at the photodetector when the incident laser beam is reflected by a glass material; Table 4.3 shows the result.

Table 4.3. Reflected power from air-glass interface incident at the photodetector.

$\Omega(MHz)$	$\theta_B = \theta_i$	$\eta_D\,\%$	$\Gamma_\perp$	$p = \eta_D \lvert\Gamma_\perp\rvert^2$	$p_D(\mu w)$
350	0.0233	8.9138	-0.2052	0.003755	93.8844
400	0.0267	7.8545	-0.2052	0.003309	82.7456
450	0.0300	6.1539	-0.2053	0.002593	64.8464
500	0.0333	7.6849	-0.2053	0.003240	81.0013
550	0.0367	10.1700	-0.2053	0.004289	107.2285
600	0.0400	15.7159	-0.2053	0.006630	165.7579
650	0.0433	5.4750	-0.2054	0.002310	57.7672
700	0.0467	100.0000	-0.2054	0.042220	1055.5212
750	0.0500	22.7839	-0.2055	0.009623	240.5907
800	0.0533	3.1709	-0.2055	0.001339	33.4988
850	0.0567	0.1915	-0.2056	0.000080	2.0238
900	0.0600	0.8881	-0.2056	0.000375	9.3921
950	0.0633	0.0086	-0.2057	0.000003	0.0906
1000	0.0667	0.0433	-0.2057	0.000018	0.4585
1050	0.0700	0.0016	-0.2058	0.0000006	0.0168

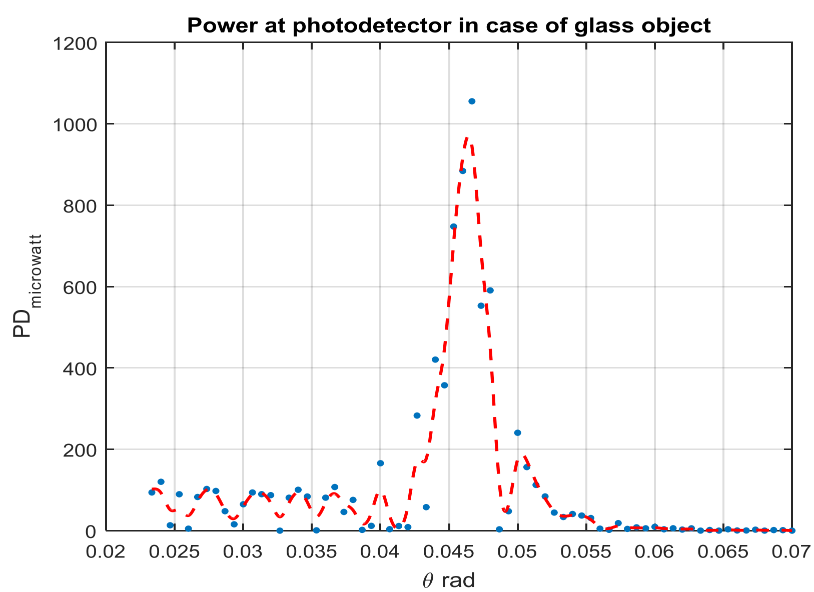

Fig.4.7. Power at the photodetector versus the scan angle for the case of glass.

Power at the photodetector is calculated when the incident laser beam is deflected from copper (which, although highly conducting, is non-magnetic).

Table 4.4. Reflected power from air-copper interface incident at the photodetector.

$\Omega(MHz)$	$\theta_B = \theta_i$	$\eta_D\,\%$	$\Gamma_\perp$	$p = \eta_D \lvert\Gamma_\perp\rvert^2$	$p_D\,(\mu w)$
350	0.0233	8.9138	0.4206	0.015773	394.3391
400	0.0267	7.8545	0.4208	0.013910	347.7610
450	0.0300	6.1539	0.4210	0.010908	272.7197
500	0.0333	7.6849	0.4212	0.013636	340.9197
550	0.0367	10.1700	0.4214	0.018067	451.7
600	0.0400	15.7159	0.4217	0.027954	698.9
650	0.0433	5.4750	0.4220	0.009752	243.8
700	0.0467	100.0000	0.4223	0.178383	4459.6
750	0.0500	22.7839	0.4226	0.040707	1017.7
800	0.0533	3.1709	0.4230	0.005674	141.9
850	0.0567	0.1915	0.4234	0.000343	8.6
900	0.0600	0.8881	0.4238	0.001595	399
950	0.0633	0.0086	0.4242	0.000015	4
1000	0.0667	0.0433	0.4247	0.000078	2
1050	0.0700	0.0016	0.4252	0.000002	1

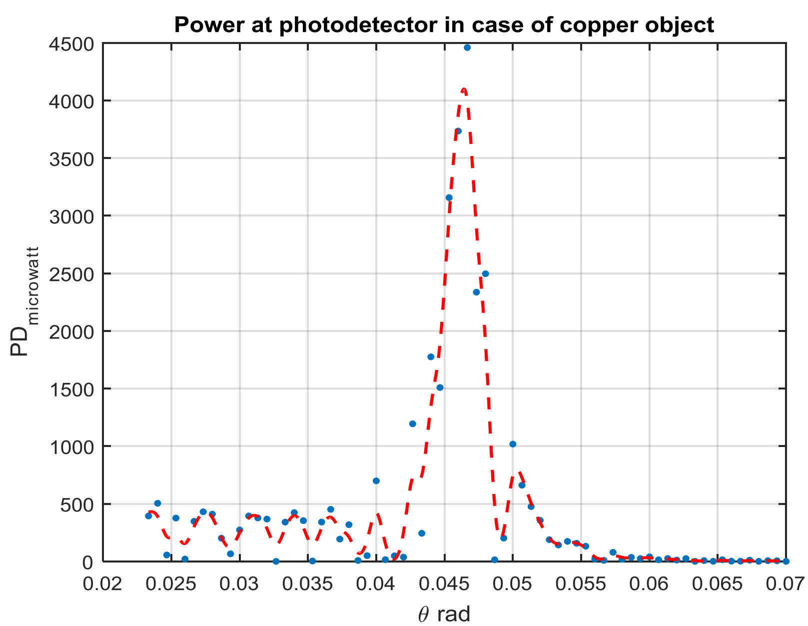

Fig.4.8. Power at the photodetector versus the scan angle for the case of copper.

Power at the photodetector is calculated when the incident laser beam deflected from aluminum (which is likewise non-magnetic) as illustrated in the following table.

Table 4.5. Reflected power from air-aluminum interface incident at the photodetector.

$\Omega(MHz)$	$\theta_B = \theta_i$	$\eta_D\%$	$\Gamma_\perp$	$p = \eta_D \lvert\Gamma_\perp\rvert^2$	$p_D(\mu w)$
350	0.0233	8.9138	-0.0660	0.000389	9.7257
400	0.0267	7.8545	-0.0660	0.000342	8.5724
450	0.0300	6.1539	-0.0660	0.000268	6.7186
500	0.0333	7.6849	-0.0660	0.000335	8.3932
550	0.0367	10.1700	-0.0661	0.000444	11.1119
600	0.0400	15.7159	-0.0661	0.000687	17.1791
650	0.0433	5.4750	-0.0661	0.000239	5.9877
700	0.0467	100.0000	-0.0661	0.004376	109.4211
750	0.0500	22.7839	-0.0661	0.000997	24.9444
800	0.0533	3.1709	-0.0661	0.000138	3.4737
850	0.0567	0.1915	-0.0662	0.000008	0.2099
900	0.0600	0.8881	-0.0662	0.000038	0.9742
950	0.0633	0.0086	-0.0662	0.0000003	0.0094
1000	0.0667	0.0433	-0.0662	0.000001	0.0476
1050	0.0700	0.0016	-0.0663	0.00000007	0.0018

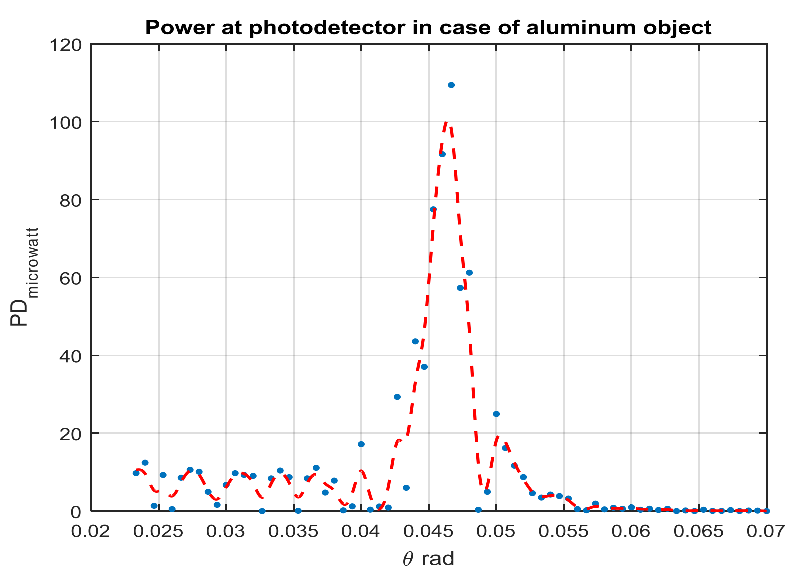

Fig.4.9. Power at the photodetector versus the scan angle for the case of aluminum.

Based on the previous table, the sensitivity of the photodetector should be greater than or equal to $0.0018\mu W$. If a photodetector does not meet this sensitivity requirement, then technically, the scan system will have to be re-designed for a shorter chirp range. We observe also that this design problem has assumed nonmagnetic interfaces throughout. In the more realistic scenario, there may well be magnetic materials present in the search, in which case a more general analysis and simulation will have to be carried out based on eqs. (15) and (17).

4.5 Horizontal and Vertical Linear Scanning Times (Δt_{ls}) and Sector Scanning Time (Δt_{ss})

The scanning time includes the linear scan time representing the time needed to cover one row with about 694 points, and the full sector scanning consisting of 694 × 600 points. The scan times are calculated numerically assuming a UAV speed of 237 m/s.

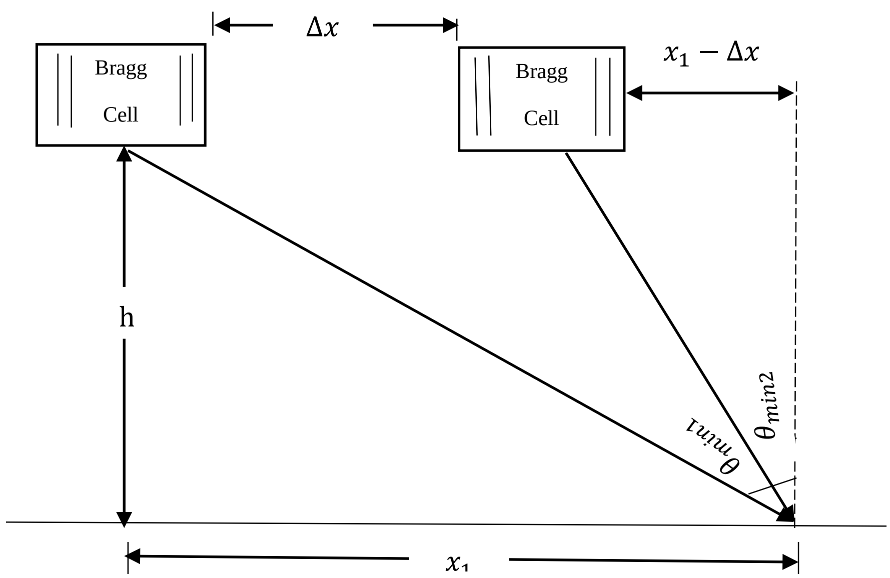

Fig.4.10. UAV movement across the scan distance.

From the above figure we get:

$$\theta_{\min 1} = \theta_B \,|_{f_{\min 1}} = \frac{\lambda}{2\Omega} = \frac{\lambda\Omega_s}{2nv_s} = \frac{\lambda f_{\min 1}}{2nv_s}, \tag{4.5a}$$

$$f_{\min 1} = \frac{2nv_s\theta_{\min 1}}{\lambda},$$

$$\theta_{\min 2} = \frac{\lambda f_{\min 2}}{2nv_s},$$

$$f_{\min 2} = \frac{2nv_s\theta_{\min 2}}{\lambda},$$

$$\frac{x_1}{h} = \tan\theta_{\min 1}, \text{ and}$$

$$\frac{x_1 - \Delta x}{h} = \tan\theta_{\min 2} = \tan\theta_{\min 1} - \frac{\Delta x}{h}\ , \tag{4.5b}$$

where, Δx is the change in the scan distance (due to UAV movement). Also,

$$\tan\theta_{\min 1} - \tan\theta_{\min 2} = \frac{\Delta x}{h}, \text{ Note that}$$

$$\theta_{\min 1} \,\&\, \theta_{\min 2} << 1 \ \ (rad)$$

$$\theta_{\min 1} - \theta_{\min 2} << 1$$

$$\theta_{\min 2} < \theta_{\min 1}$$

$$(\theta_{\min 1} - \theta_{\min 2}) \approx \theta_{\min 1} = 23.34\, mrad\ ,$$

$$\frac{\Delta x}{h} << 23.34\ mrad, \text{ and}$$

$$\Delta x\ = 23.34 \times 10^{-3} \times h\,.$$

$$\because h\ = 8km\ \ ,$$

$$\Delta x\ = v\ \times n \times \Delta t_{ls}\,,$$

$v \times n \times \Delta t_{ls} << 23.34 \times 10^{-3} \times 8 \times 10^{3}$,

$v \times n \times \Delta t_{ls} << 186.72$, where $v = 237 \, {}^{m}\!/_{s}$ (v is the UAV speed).

Since, the height of the unit cell scan sector is $300m$, and the laser spot in size of $1m$ moves by $0.5m$ on the ground then the number of linear scan lines in one sector $n = 600$

$$\Delta t_{ls} << \frac{186.72}{237 * 600} \Rightarrow \Delta t_{ls} << 0.0013ms \approx 1.3131\mu s$$

(1) Scan time for horizontal sector

Linear scan time $\Delta t_{ls} = 1\mu s$

Sector scan time $\Delta t_{ss} = n \times \Delta t_{ls} = 600 \times 1\mu s = 0.6ms$

(2) Scan time for vertical sector

$$\Delta t_{ls} << \frac{186.72}{237 * 1200} \Rightarrow \Delta t_{ls} << 6.5654 \times 10^{-4} ms \approx 0.6565\mu s$$

Linear scan time $\Delta t_{ls} \approx 0.3\mu s$.

Sector scan time $\Delta t_{ss} = n \times \Delta t_{ls} = 1200 \times 0.3\mu s = 0.36ms$

Table 4.6. Scan times for horizontal and vertical sectors.

Horizontal sector		Vertical sector	
Linear scan time	Sector scan time	Linear scan time	Sector scan time
1 μs	0.6 ms	0.3 μs	0.36 ms

Note that it is reasonably straightforward to show that the scan times are considerably lower than the propagation time of the UAV across the sectors. Hence the scan operation occurs much faster than it takes for the UAV to enter the scan area. This enables the juxtaposition of horizontal and vertical scans in each unit cell. Within each sector, the Bragg cell will rotate in a series of steps via the stepper motor; subsequently it must rotate by 107^0 prior to executing the vertical scan. Note that the need to rotate the Bragg cell in the μs time range will require a sufficiently high speed motor- which may require the use of a piezo-motor instead of the stepper motor.

Table 4.7. Bragg cell rotation angles.

Horizontal sector					Vertical sector			
Rotation each step (CCW)	Time	Complete rotation (CW)	Time	One rotation (CCW)	Rotate each step (CW)	Time	Complete rotation(CW)	Time
0.051^{o}	1 μs	30.66^{o}	0.6 ms	107.1384^{o}	0.051^{o}	0.3 μs	63.7577^{o}	0.36 ms

4.6 Simulation Results

A simulation of the scanning system shown in Fig.5.1 is implemented in MATLAB and the results are presented in this section. The simulation is created based on four randomly distributed materials with different refractive indices in sea water in size of 30kmx30km as shown in Fig.11.

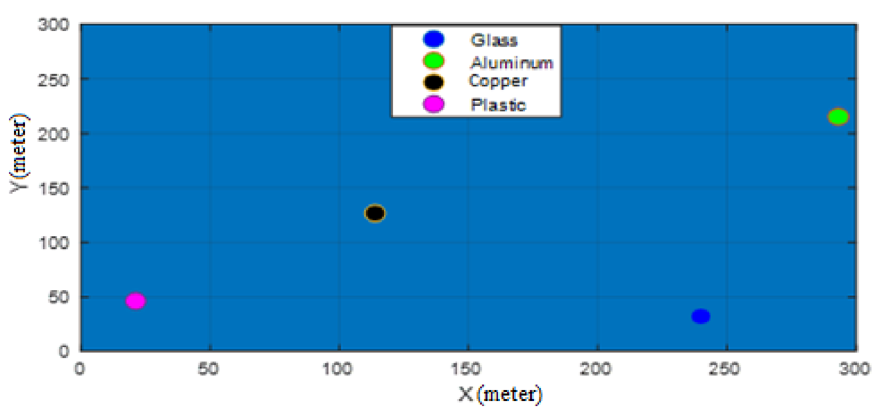

Fig.4.11. Four randomly distributed materials with different refractive indices.

Fig.4.11 shows 4 random objects on the scan surface identified by the scan algorithms using the methodology described above. Upon identifying a "hit," the UAV is programmed to transmit to a ground station the coordinates of the scanned "object" following which a ground-based rescue vessel may proceed with retrieval of the "object." The refractive index is unique for each material and it depends on some parameters such as that the frequency of the electromagnetic wave and the operating temperature [30]. The refractive index needs to be known in order to identify the material; Table.4.8 show the refractive index of the chosen material at the red laser frequency $0.632\mu Hz$.

Table.4.8. Refractive index of chosen material at $0.632\mu Hz$.

Material	Wavelength (μm)	Refractive index
Glass	0.632	1.5163
Aluminum	0.632	1.1414
Copper	0.632	0.40835
Plastic	0.632	1.4901

Amplitude of the refractive index of the martial that chosen to be detected including the interface (seawater) versus the reflection coefficient is shown in the next figure.

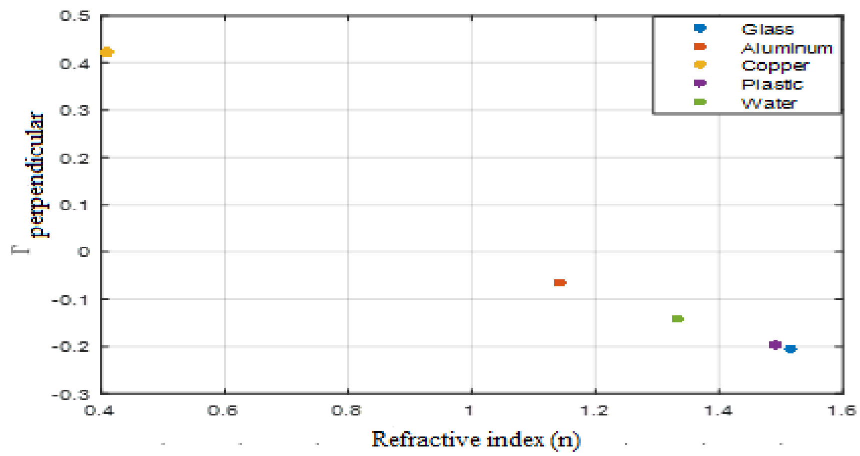

Fig.4.12. Five distinct materials identified via the scan algorithm showing amplitude reflection coefficient and corresponding refractive indices.

Fig. 4.12 shows the reflection coefficients for four different materials relative to their refractive indices. It needs to be mentioned here that the physical design carried out in this work is based on a few important assumptions. Some of these are:

(1) All the materials involved are nonmagnetic in nature;

(2) The surface containing the objects is entirely planar; hence, this system would need significant modifications if non-planar surfaces are involved;

(3) It is known that at certain wavelengths, materials may begin to dielectric losses (i.e., their permittivities and/or permeabilities may begin to become complex). For copper, for instance, at visible wavelengths, the permittivity may in fact be complex (and hence introduce dielectric loss in the system) in such a situation, the reflective properties may involve further power loss. Moreover, for the materials graphed in Fig.4.12, *only copper shows a (real) refractive index less than 1*. This may have a certain correlation with plasmonic phenomena [31];

(4) Alternative remote object scanning methodologies (such as the common use of electro-optic scanning methods) exist which might possess certain advantages over the method used here, but these have not been pursued in this research.

The laser beam reaching the seawater is designed to be 1 m wide and moves in increments of 0.5 m to ensure overlap the spots on the ground to increase the covered scanning area; therefore, it is expected to detect objects within a 1m diameter or less, which are typical numbers for a debris field. As discussed, the photodetector mounted outside the UAV will capture the reflections and thereafter send the coordinates (XY) of non-seawater objects to ground control, thereby physically locating the object. If any reflection matches that of seawater reflection, the photodetector will notify a failed scan. The scan logarithm is applied on five random materials, and the actual coordinates of each material is calculated and compared with the scan coordinates as distributed in the next table.

Table 4.9. Retrieved versus the true coordinates of 4 randomly selected objects within the scan area.

Real Coordinates	Scanned/retrieved Coordinates
(240, 32)	(239.89, 32.00)
(21, 46)	(20.99, 45.91)
(114, 127)	(113.99, 126.80)
(293, 215)	(293.07, 215.22)

As can be seen from Table 4.9, the error between the actual and scanned coordinates is very small, and this indicates a relatively accurate scan model. To test the accuracy of the scan algorithm three materials identified by the scan algorithm are shown within the scan area in Fig.4.13.

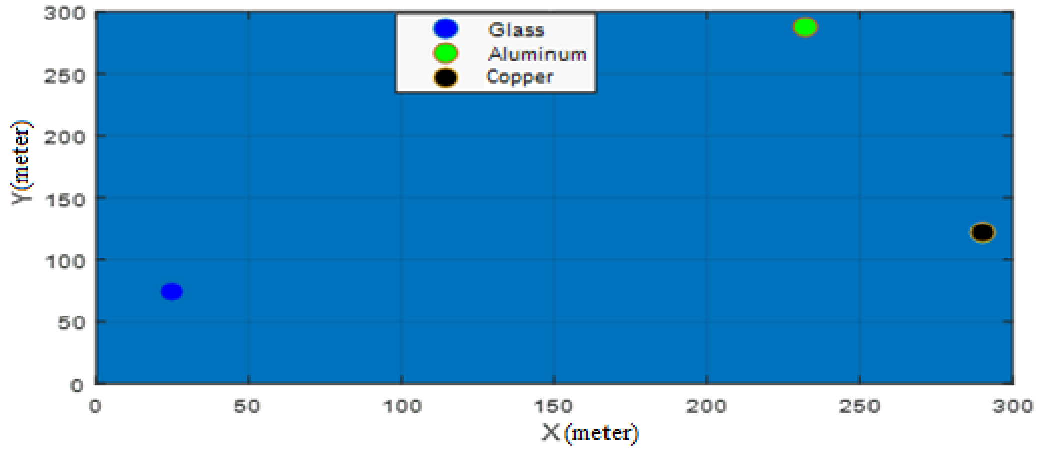

Fig.4.13. Three random distribution materials with different refractive indices.

Table 4.10. Real and retrieved coordinates for scanning system.

Real Coordinates	Scanned/retrieved Coordinates
(290, 122)	(289.77, 121.92)
(25, 74)	(24.96, 73.95)
(232, 288)	(231.80, 287.86)

As can be seen from Table.4.10 the scan model works reasonably well and is able to identify the object's coordinates with high accuracy, indicating the reliability of the scan model.

CHAPTER 5

CONCLUSION AND FUTURE WORK

Design and numerical demonstration of a scanning system using a Bragg cell excited by a chirped RF source are presented in this research. There are some limitations with this design such as the scan model is valid with a uniform plan surface (i.e. sea surface, desert) and nonmagnetic media as well as perpendicular polarization. The reason for choosing perpendicularly polarized light for the scanning problem is to avoid any possible Brewster condition during the reflection from the scanned surface, since the detection of the reflecting material is based on measuring the reflected light. The scan model is applied on four materials with different refractive indices randomly distributed on a seawater background, and they are perfectly detected. The reflection coefficient of a laser beam on an object is shown to depend on the angle of incidence, beam frequency and material constants such as refractive indices. The optimal Bragg cell length delay is determined in such a way to ensure Bragg operation throughout the chirp range. The chirp frequency is designed to be within the range 350 MHz to 1050 MHz; the corresponding Bragg angles are in the mrad range leading to high angular resolution. The scanning systems including the Bragg cell is carried on board a UAV operating in the XZ plane, and is designed to scan the horizontal surface (XY plane). Vertical and horizontal sectors are created to cover all the scan area. Double (or higher) scanning may occur for any object located within overlapping scan sectors. A photodetector mounted on the outside the UAV is shown to be active throughout the scanning area. The photodetector is combined with electronics which transmit either a failed scan or the coordinates of any object with refractive index different from seawater reflection to ground control as well as send a signal to the stepper motor to rotate the Bragg cell by pre-selected angles after each scan line. The scanning system is simulated via MATLAB and the results indicate high accuracy. The scan model is designed to cover scan area of 30km × 30km. The UAV makes wide 180^0 turns at the end of each row scan (30km).

Future work:

This work could be extended to include the following objectives:

(1) The scan system modified to be valid if non-planar surfaces are involved

(2) Extend the scan algorithm to be used for magnetic material detection.

(3) Further algorithm may developed to reach higher accuracy and faster scanning times.

REFERENCES

[1] V.V. Nikulin, R.M. Khandekar and J. Sofka, “Agile acousto-optic tracking system for free space optical communications,” Opt. Eng. 47(6), 064301 (2008).

[2] L.H. Gesell, R.E. Feinleib, J.L. Lafuse and T.M. Turpin, “Acousto-optic control of time delays for array beam steering,” Proc. SPIE, vol. 2155, pp.194-204, June 1994.

[3] A. Korpel, “Acousto-Optics,” 2nd edition, Marcel Dekker, New York, (1997).

[4] G. C. Giakos, “Multifusion multispectral lightwave polarimetric detection principles and systems,” IEEE Transactions on Instrumentation and Measurement 55, 1904-1912 (2006).

[5] S. Sumrain and G. C. Giakos, “Efficient polarimetric detection of man-made targets,” IEEE International Workshop on Imaging Systems and Techniques, pp. 20–25 (2006).

[6] A. Wehr and L. Uwe, “Airborne laser scanning- an introduction and overview,” ISPRS J. of Photogram. and Rem. Sensing 54(2), 68-82 (1999).

[7] C.A. Balanis, *Advanced Engineering Electromagnetics*, 2nd Ed., Wiley, NY (2014).

[8] C.D. Tran, “Acousto-optic devices, optical elements for spectroscopy,” Analyt. Chem. 64, 971–981 (1992).

[9] P. Debye, and F. W. Sears, "On the scattering of light by supersonic waves," Proc. Nat. Acad. Sci. USA 18, 409-414 (1932).

[10] R. Lucas, and P. Biquard, "Optical properties of solid and liquid medias subjected to high-frequency elastic vibrations," Jour. de. Phys. et Rad. 3, 464- 477 (1932).

[11] A. Korpel, "Selected Papers on Acousto-Optics," SPIE Milestones Series, 16, 73-78 (1990).

[12] W.L. Bragg, "The diffraction of short electromagnetic waves by a crystal," Proc. Camb. Phil. Soc. 17, 43-75 (1913).

[13] W.R. Klein and B.D. Cook, "Unified approach to ultrasonic light diffraction," IEEE Trans. Sonics Ultranson. SU-14, 123-133 (1967).

[14] S.-T. Chen, and M.R. Chatterjee "A numerical analysis and expository interpretation of the diffraction of light by ultrasonic waves in the Bragg and Raman-Nath regimes multiple scattering theory," IEEE Trans. on Education 39(1), 56-68 (1996).

[15] A. Korpel and T.-C. Poon, "Explicit formalism for acousto-optic multiple plane wave scattering," J. Opt. Soc. Am. 70, 817–820 (1980).

[16] A.W. Rihaczek, "Principles of High-Resolution Radar," McGraw-Hill, New York (1969).

[17] W.R. Klein and B.D. Cook, "Unified approach to ultrasonic light diffraction," IEEE Trans. Sonics Ultrason. SU-14, 123–133 (1967).

[18] A. Korpel and T.-C. Poon, "Explicit formalism for acoustooptic multiple plane-wave scattering," J. Opt. Soc. Am., 70, 817–820 (1980).

[19] W.R. Klein, “Light diffraction by ultrasonic beam of high frequency near Bragg angle,” Proc. 5th Congress Int. D’ Acoustique, Liege, Belgium, D24 (1965).

[20] W.L. Bragg, “The diffraction of short electromagnetic waves by a crystal,” Proc.Camb. Phil. Soc. 17, 43-75 (1913).

[21] T.-C. Poon and A. Korpel. “Optical transfer function of an acousto-optical heterodyning image processor,” Opt. Lett. 4(10), 317-391 (1979).

[22] V. Minier, A. Kervorkian, and J.M. Xu, “Diffraction characteristics of superimposed holographic gratings in planar optical waveguides,” IEEE Photon. Tech. Lett. 4(10), 1115-1118 (1992).

[23] W.R. Klein and B.D. Cook, “Unified approach to ultrasonic light diffraction,” IEEE Trans. Sonics Ultrason. SU-14, p. 123 (1967).

[24] J. Chrostowski and C. Delisle, “Bistable piezoelecβc Fabry–Perot interferometer,” Can. J. Phys., 57, 1376-1379 (1979).

[25] A. Korpel and T.-C. Poon, “Explicit formalism for acousto-optic multiple plane-wave scattering,” J. Opt. Soc. Am. 70, 817–820 (1980).

[26] T.-C. Poon and T. Kim, *Engineering Optics with MATLAB*. World Scientific, Singapore (2006).

[27] C.A. Balanis, *Advanced Engineering Electromagnetics*, 2nd Ed., Wiley, NY (2014).

[28] S.J. Orfanidis. Electromagnetic waves and antennas. Online Book, http://www.ece.rutgers.edu/ orfanidi/ewa/, 2008.

[29] M.R. Chatterjee, T-C. Poon, and D.N. Sitter, Jr., “Transfer function formalism for strong acousto-optic Brag gdiffraction of light beams with arbitrary profiles,” Acustica 71(2), 81-92 (1990).

[30] G. N. Ramachandran, in Progress in Crystal Physics, Volume 1, edited by R. S. Krishnan, lnterscience Publishers, New York, London, pp. 139- 167 (1958).

[31] P.P. Banerjee, *private communication.*